High energy and excellent stability asymmetric supercapacitor derived from sulphur-reduced graphene oxide/manganese dioxide composite and activated carbon from peanut shell

Delvina Japhet Tarimo, Kabir O. Oyedotun, Abdulmajid A. Mirghni, Ndeye Fatou Sylla and Ncholu Manyala*.

Department of Physics, Institute of Applied Materials, SARChI Chair in Carbon Technology and Materials, University of Pretoria, Pretoria 0028, South Africa.

*Corresponding author's email: ncholu.manyala@up.ac.za, Tel.: + (27)12 420 3549.

HIGHLIGHTS

• RGO-S and RGO-S/MnO$_2$ composites were successfully synthesized.

• Electrochemical performance of RGO-S/MnO$_2$ has been improved by introduction MnO$_2$.

• The RGO-S/MnO$_2$ was adopted as positive electrode in asymmetric device.

• The fabricated device proves to be of great potential for supercapacitors applications.

ABSTRACT

Nanorods/fibers, nanosheet and nano-flower like structure were effectively synthesized from sulphur-reduced graphene oxide (RGO-S) and sulphur-reduced graphene oxide/manganese dioxide (RGO-S/MnO$_2$) composites for supercapacitor applications. Structural, chemical composition and morphological analysis reveal an effective synthesis of the RGO-S and RGO-S/MnO$_2$ composite. Electrochemical measurements of the optimized mass loading of MnO$_2$ on RGO-S in a three electrode configurations revealed a specific capacitance of 180.4 F g^{-1} compared to 75.2 F g^{-1} of the pristine sample at 1 A g^{-1} in 2.5 M KNO$_3$ electrolyte. An assembled asymmetric device consists of optimized RGO-S/MnO$_2$ as positive electrode and activated carbon from peanut shell (AC-PS) as a negative electrode delivered a high specific energy of 71.74 Wh kg^{-1} with its corresponding specific power of 850 W kg^{-1} at 1 A g^{-1}. It was observed that even at high specific current of 5 A g^{-1} the device was able to maintain a specific energy of 55.30 Wh kg^{-1}. An excellent stability with capacitance retention of 94.5 % and columbic

efficiency of 99.6 % up to 10, 000 cycles was recorded for the device at 5 A g^{-1}. The device demonstrated a very good stability after being subjected to a voltage holding of up to 90 h and an outstanding self-discharge of about 1.45 V was recorded within the first 10 h and 1.00 V after 72 h from its maximum potential of 1.7 V.

GRAPHICAL ABSTRACT
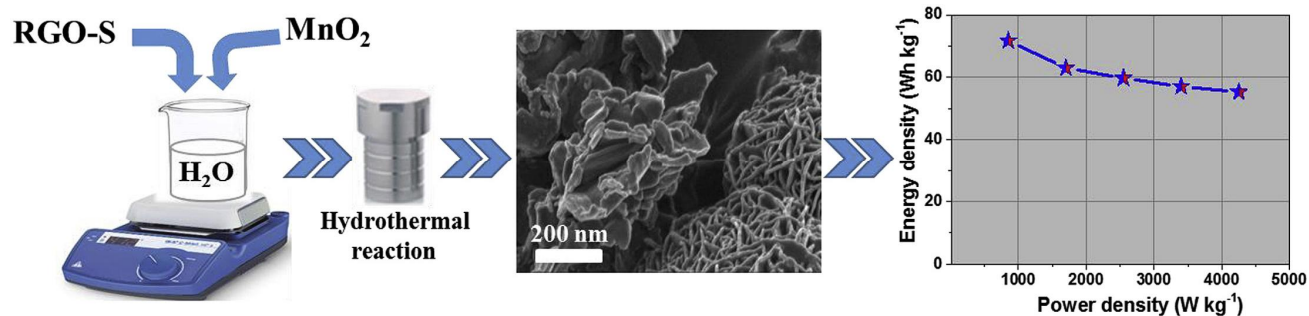
KEY WORDS: Sulphur-reduced graphene oxide, hybrid device, energy density, supercapacitor, shuttle effects, composite materials

1. INTRODUCTION

The variations in precipitation, sea level and rising temperature will affect how much energy is produced, delivered and consumed. Due to a huge effect caused by climate change and high consumption of fossil fuels which is limited and has environmental problems like green-house effect, there is a need to find an alternative energy source. Renewable energy is the energy harvested from natural resources such as geothermal energy, solar, hydropower and wind. However, energy harvested from these resources is not available all the time because it depends on the weather and time. For example, solar energy can only be harvested during the day time, so in order to have sufficient energy, energy storage devices like supercapacitors, battery and other energy conversion systems are required [1–6].

Recently, the supercapacitor has attracted most research community owing excellent cycling stability, high power density and fast charge/discharge ability [2,7–9]. By considering the charge storage mechanism, the supercapacitor is characterized as the electric double-layer capacitor (EDLC) and faradic/pseudo capacitor. EDLC store energy through the separation of charges in a Helmholtz double layer at the interface of electrode and electrolyte while pseudo/faradic capacitor its storage is achieved by a redox reaction between the electrode and the electrolyte [10–14].

For innovative energy storage devices (supercapacitor), microstructure has effect on the electrochemical performance of electrode materials [15–17]. This makes scientists focus on developing new materials which can meet energy demands. Mostly, carbonaceous materials such as activated carbon, carbon aerogel, graphene and carbon nanotube store energy through reversible adsorption-desorption of ions on the surface of the electrode leading to high power density and long cycle life but low energy density [4,18–22]. The use of dopants such as boron (B), phosphorus (P), sulphur (S) and nitrogen (N) has seen to enrich physical and chemical properties like wettability of the carbonaceous materials [2,10,23,24]. Precisely, the synthesis of sulphur carbonaceous materials for supercapacitor is of great importance due to its ability to create redox active sites by attracting the greater number of electrons which in turn increases the capacity/capacitance of the material [1,11,21,25]. However, shuttle effects occur during the conversion of sulphur to different sulphides products, makes supercapacitor to suffer from poor stability during a long cycling process [6,26–30]. Several approaches have been attempted to resolve the problem, which include binding the material onto conducting polymers [3,31], metal hydroxides [7], metal oxides [12] and metal sulphides [32] hosts which derives its capacitance from redox reaction that occurs between or on the surface of the electrode which proves to have a high energy density [16,27,33]. These material hosts offer high efficiency of chemisorption, which suppress polysulphide diffusion by improving the long term stability through the creation of strong chemical adsorption and immobilize the polysulphide species.

Recently, the varieties of d-block metals and their oxides such as cobalt oxide, manganese dioxide (MnO_2), tin oxide and nickel oxide, have been used as a well-established active electrode for supercapacitor due to several oxidation states and pseudocapacitive behaviour [4,20,33–35]. MnO_2 has been regarded as a high standard electrode material for supercapacitor applications, owing to high specific capacity/capacitance, variable oxidation state, abundant availability/low cost and non-toxicity. Since MnO_2 exits in different polymorphs, it can be tuned to produce different crystallography structure and morphological properties which in turn can change the electrochemical properties via doping or composites formation [3,9,29,36,37]. The material has the ability to grow within or around the carbon matrix, thus serves as a highly effective sulphur host which offers strong face-to-face entrapment, greatly maintaining the polysulphide and improves cycling stability over a long cycles.

In this study, sulphur-reduced graphene oxide/manganese dioxide composite was synthesized for supercapacitor applications. The electrochemical performance of the material was evaluated using both three- and two-electrode configurations in 2.5 M KNO_3 electrolyte. The RGO-S/100 mg MnO_2 composite measured as a half-cell revealed a peak specific capacitance of 180.4 F g^{-1} at 1 A g^{-1}. The fabricated RGO-S/100 mg MnO_2//AC-PS asymmetric hybrid device using RGO-S/100 mg MnO_2 and activated carbon from peanut shells (AC-PS) demonstrated high energy density of about 71.74 Wh kg^{-1} with its corresponding power density of 850 W kg^{-1} at a specific current of 1 A g^{-1}. The material was able to retain about 94.5 % of its initial capacitance, with a columbic efficiency of 99.6 % at 5 A g^{-1} for over 10, 000 cycles. Also, the device proved its stability in long cycling after being able to stand a voltage holding test for up to 90 h and preserving a 1.45 V of its maximum potential after a self-discharge test for the first 10 h, and a 1.00 V after 72 h in an open circuit.

2. EXPERIMENTAL

2.1 Synthesis of sulphur-reduced graphene oxide (RGO-S)

RGO-S was synthesized by mixing 1 g of sulphur and 3 g of sodium sulphide (Na_2S) into 100 mL of deionized (DI) water. The mixture was sonicated until a homogenous solution was formed labelled sample **A**. Then, sample **B** was formed by dissolving 50 mg of L-ascorbic acid into 12 g of DI water, followed by addition of 2 mL of hydrochloric acid (HCl). Thereafter, 3 g of as-prepared RGO (details in the supporting information, S1 [[38–40]]) and sample **B** were mixed and then added into sample **A**. The resulting mixture was sonicated for 2 h and then stirred at 40 °C for 1 h. Thereafter, the mixture was allowed to settle down naturally for about 12 h. It was washed several times with DI water, centrifuge three times at 10,000 rpm for 10 min and later freeze-dried for 24 h.

2.2 Synthesis of manganese dioxide (MnO_2)

0.5 g of $KMnO_4$ was liquefied into 60 mL of DI water and stirred at 150 revs/min for 10 min. Subsequently, 2 mL of HCl was added dropwise and stirred for 10 min in air. The solution was transferred into 100 mL autoclave and heated in the oven at 130 °C for 1 h. The procedures were repeated at different dwell times of 2 h, 5 h, 8 h and 11 h respectively. The solution was left to cool down naturally and then washed several times with the mixture of DI water and ethanol to remove the impurities. The sample was dried in the oven for 12 h at 60 °C.

2.3 Synthesis of the composite sample (RGO-S/MnO_2)

1 g of RGO-S was liquefied into 80 mL of DI water to form a solution which was stirred at 200 revs/min for 10 min for homogeneity. Thereafter, 50 mg of MnO_2 prepared for 1 h was added into the solution and then stirred for 5 min. The procedures were repeated by different masses of MnO_2 synthesized for 1 h (100 mg and 150 mg). The suspension was transferred into the

autoclave and then heated in the oven at 150 $^{\circ}$C for 1 h. The solution was left to cool down to room temperature, washed several times with DI water and then dried in the oven for 12 h.

2.4 Synthesis of activated carbon from peanut shell waste (AC-PS)

The activated carbon nanostructure employed in this study was synthesized as per our previous work [41]. Briefly, the material was synthesized using two steps at elevated temperature. First, pyrolysis of the raw material from peanut shell waste was done at 600 $^{\circ}$C for 2 h under argon atmosphere. Thereafter, potassium hydroxide (KOH) as an activating agent and peanut shell waste as a raw material were mixed together in a mass ratio of 4:1 and activated at 850 $^{\circ}$C for 1 h. The obtained product was named as AC-PS.

2.5 Characterization

The morphology and elemental composition of the as-synthesized material was examined by the scanning electron microscope (SEM-Zeiss Ultra Plus 55 field emission scanning electron microscope operated at 2.0 kV; Akishima-shi, Japan) equipped with an energy-dispersive X-ray (EDX) and a high resolution transmission electron microscope (HRTEM FEI Tecnai-F30 operated at 1.0 kV); (Akishima-shi, Japan). X-ray diffraction (XRD - Bruker BV 2D PHASER Best Benchtop); (PANalytical BV, Amsterdam, Netherland) with reflection geometry at 2θ values (5 - 90°) in a step size of 0.005° using Cu K_{α_1} radiation source ($\lambda = 0.15406\ nm$) at 50 kV and 30 mA, was used to analyse the phase structures of the material. The functional group of the material was determined by using a Fourier transmission-infrared (FTIR) achieved via Varian FT-IR spectroscopy ranging 400 - 4000 cm^{-1} in wavenumber.

2.6 Electrochemical characterization

Two- and three-electrode configuration measurements were performed by a Bio-Logic VMP300 potentiostat (Knoxville TN, USA) operating on the EC-Lab VI.41 software. The electrodes were prepared by mixing 80 % of the sample as working material, 10 % conductive carbon acetylene (CAB) and 10 % of polyvinylidene (PVDF) as the binder. Few drops of 1-methyl 2-pyrollidone (NMP) was added to the mixture to form slurry, which was pasted onto a nickel form, 1.0 x 1.0 cm^2 and thickness-diameter of 0.2 by 16 mm serving as current collector for three and two-electrode respectively. The electrodes were dried in the oven at 60 $^{\circ}$C for 12 h. All electrochemical measurements were carried out using 2.5 M KNO$_3$ aqueous electrolyte. The 2.5 M KNO$_3$ was chosen as electrolyte because it is environmentally friendly, non-corrosive and has high conductivity hence revealed better electrochemical performance compared 1 M Na$_2$SO$_4$, 1 M KOH, 1 M H$_2$SO$_4$ and 1 M KNO$_3$ as shown in Fig. S6 in the supporting information. This performance might be contributed by the stability and pH of the electrolyte which makes it to operate in a wider potential window unlike acidic/alkaline electrolyte which is limited by oxygen evolution reaction (OER) and hydrogen evolution reaction (HER). The fabricated electrodes were tested using cyclic voltammetry (CV), galvanostatic charge discharge (GCD) and electrochemical impedance spectroscopy (EIS), respectively.

3. RESULTS AND DISCUSSION

The morphology and elemental analysis of the as-synthesized RGO-S (pristine sample) with its composites are shown in Figs. 1 and 2, respectively. Fig. 1 (a, b) shows low and high magnifications SEM images of RGO-S confirming the formation of nanorods/nanofibers and nanosheet morphologies. The formation of these morphologies were contributed by the addition of sulphur and the long-chained ascorbic acid [25,42,43]. Fig. 1 (c) shows a TEM

image for RGO-S which confirms what was observed from the SEM analysis. Figs. 1 (d, e) shows low and high magnifications SEM images of MnO_2 flower like morphology synthesized for 1 h with its corresponding TEM image in Fig. 1 (f). Since integration of external additives is expected to affect chemical and physical properties of the composites, thus variation of masses of the MnO_2 sample become necessary. Besides, conductivity and the resultant capacitance of RGO-S and MnO_2 composites can be improved by investigating their ratio. Fig. 1 (g, h, j, k, m, and n) displays the SEM images of RGO-S/MnO_2 composites at different mass loading of MnO_2 with their corresponding TEM micrograph in Fig. 1 (i, l and o), respectively. It was observed that all the three composite samples (50, 100 and 150 mg) revealed similar morphologies comprising nanosheets, nanorods and nanoflowers like particles. The RGO-S/100 mg MnO_2 composite was noticed to be consisting of visible porous structure, which is expected to allow for more effective passage of electrolyte ions within the material as compared to the RGO-S/50 mg MnO_2 and RGO-S/150 mg MnO_2 samples. For RGO-S/150 mg MnO_2, the morphology looks non-porous hence the movement of ions from the electrolyte within the material is expected to be not so great which should lead to poor electrochemical performance. EDX analysis was used to determine the elemental composition of the as-synthesized RGO-S and RGO-S/MnO_2 composites with different mass loading of MnO_2. Fig. 2 (a) shows EDX analysis of RGO-S confirming the presence of individual elements C, S, O, while Fig. 2 (b) shows Mn and O in the MnO_2 sample. Fig. 2 (c – e) confirm the existence of C, S, O and Mn in the RGO-S/MnO_2 composites. The observed K in the spectrum of MnO_2 is due to the potassium per manganite ($KMnO_4$) chemical used during the sample synthesis.

Fig. S7 (a, b) in supporting document displays SEM images of pristine RGO at low and high magnifications, respectively. The RGO without sulphur doping reveals a sheet like morphology as already indicated and discussed in our previous work [40].
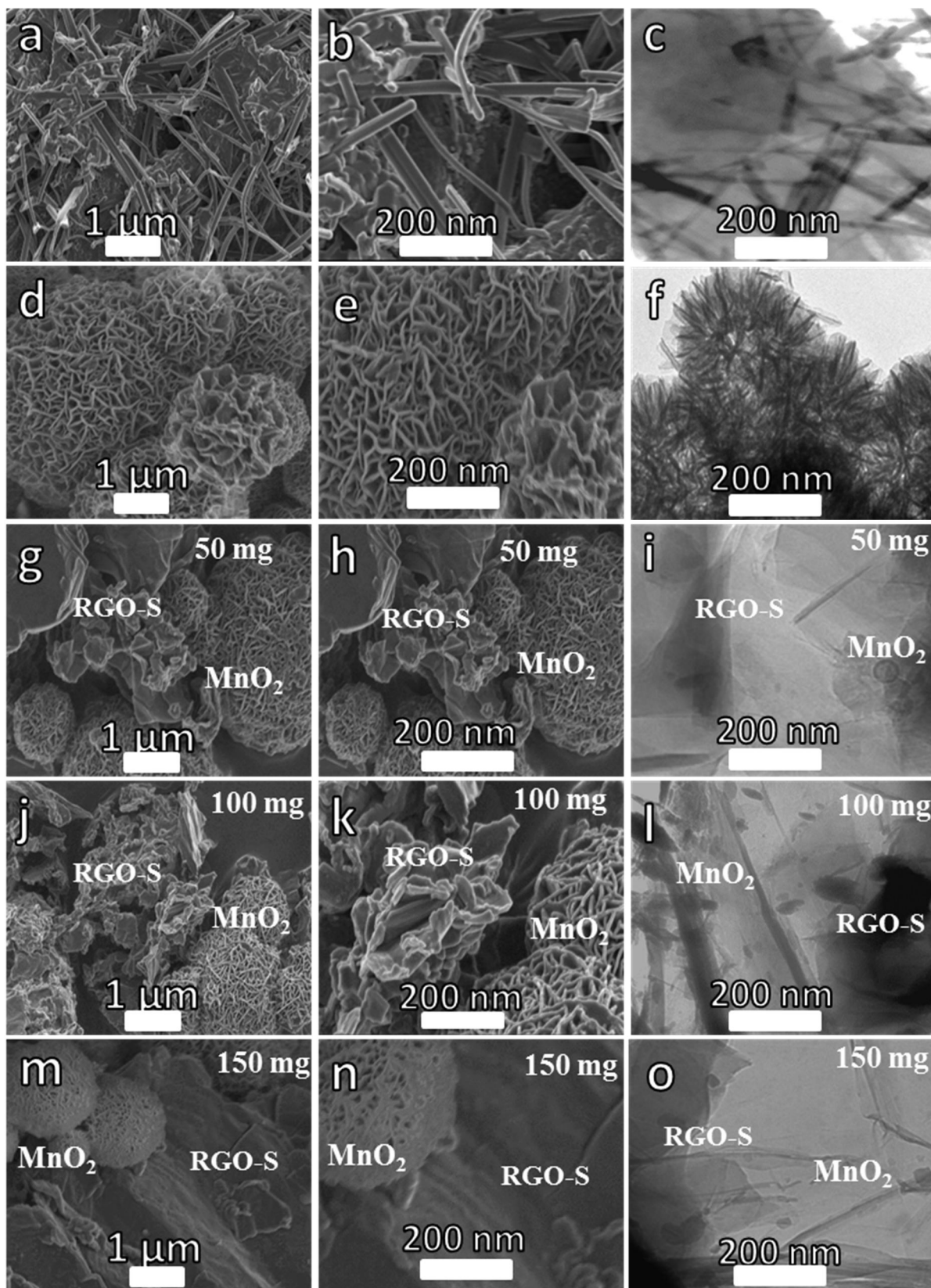
Fig. 1: (a, b), (d, e): SEM images of RGO-S and MnO_2 respectively and (g, h) (j, k) and (m, n): SEM images for RGO-S/50 mg MnO_2, RGO-S/100 mg MnO_2 and RGO-S/150 mg MnO_2 at low and high magnifications, respectively. (c, f, i, l and o) are TEM images for RGO-S, MnO_2, RGO-S/50 mg MnO_2, RGO-S/100 mg MnO_2 and RGO-S/150 mg MnO_2, respectively.
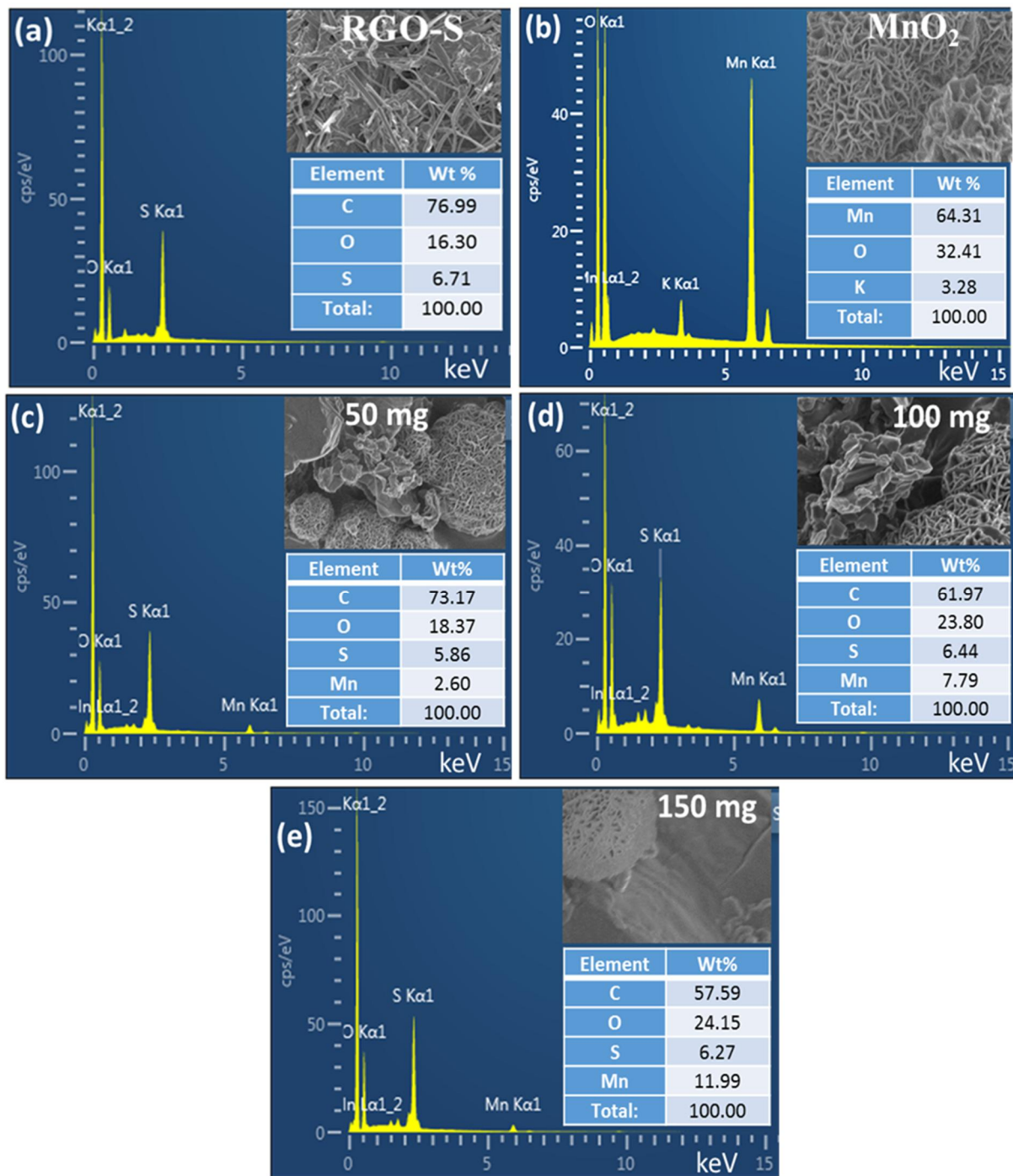
Fig. 2: EDX for (a) RGO-S, (b) MnO₂, (c) RGO-S/50 mg MnO₂, (d) RGO-S/100 mg MnO₂ and (e) RGO-S/150 mg MnO₂, respectively.

Fig. 3 (a) displayed the XRD spectrum for the as-synthesized RGO-S (pristine), MnO₂, RGO-S/50 mg MnO₂, RGO-S/100 mg MnO₂ and RGO-S/150 mg MnO₂ shown crystal structure and phase purity of the samples. Both samples revealed a crystallinity structure measured between the angular range $2\theta = 5^\circ – 90^\circ$. The monoclinic crystal structure of RGO-S corresponds to the

10

matching card no. JCPDS N34-0941 [44] while that of MnO_2 are in line with the α-MnO_2 card no. JCPDS 00-044-0141 [18,45]. The XRD spectrum around 12.5 º, 27.6 º, 23.08º and 42.4º corresponds to (002), (331), (222) and (319) planes respectively, displaying the existence of C and S in the RGO-S matrix, respectively. The presence of peaks around 12.1º, 24.6º, 36.5º and 65.7º which corresponds to the α-MnO_2 (110), (220), (211) and (002), planes respectively, conforms to the successful incorporation of α-MnO_2 into RGO-S/MnO_2 composites. The FTIR analysis of the RGO-S (pristine), MnO_2, RGO-S/50 mg MnO_2, RGO-S/100 mg MnO_2 and RGO-S/150 mg MnO_2 is shown in Fig. 3 (b). Bending vibrations of hydroxyl groups and stretching vibrations of interlayer water molecules was observed around 1741 cm^{-1} bands. The peak around 1218 cm^{-1} was assigned to the interaction of Mn with the host species [15].
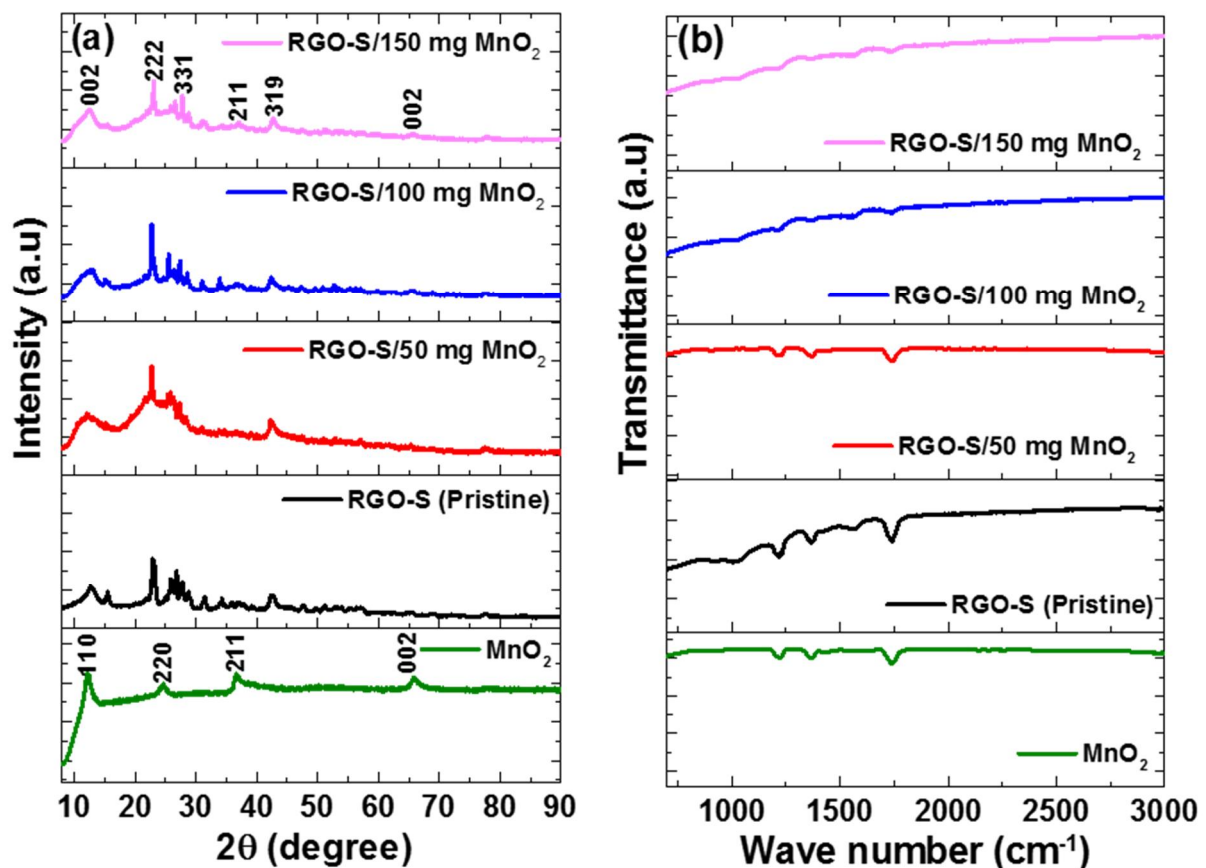

Fig. 3: (a) XRD and (b) FTIR for RGO-S (Pristine), MnO_2, RGO-S/50 mg MnO_2, RGO-S/100 mg MnO_2 and RGO-S/150 mg MnO_2, respectively.

The as-synthesized sample was evaluated for electrochemical measurements in a three-electrode configuration using Ag/AgCl as reference electrode and glassy carbon as the counter electrode in 2.5 M KNO_3 aqueous electrolyte. Fig. S2 (a) indicates an electrochemical evaluation in a positive potential window range of 0.0 - 0.6 V vs Ag/AgCl through cyclic voltammetry (CV) for the RGO-S (pristine) sample at different scan rates, which shows a rectangular shape that reveals an electric double layer capacitor (EDLC) behaviour. This was further confirmed by a symmetric triangular shape possessed by the galvanostatic charge-discharge profile as shown in Fig. S2 (b). Furthermore, to make an evaluation of the composite material an additive manganese dioxide (MnO_2) was prepared by varying hydrothermal dwelling time. The electrochemical measurements in a positive potential window range of 0.0 - 0.6 V vs Ag/AgCl revealed that 1 h dwelling time performed better compared to the rest of the dwelling times as shown in Fig. S3 (a-c). Therefore, 1 h preparation of the additive MnO_2 was chosen to prepare RGO-S/MnO_2 composites by varying the mass of MnO_2. MnO_2 is one of the classic pseudocapacitive material which will possibly increase the capacitance of RGO-S, while the RGO-S is expected to provide or improve the conductivity of the material and at the same time contributed to the sample's pseudocapacitive behaviour. Sulphur is an attractive material for energy storage devices owing to its high theoretical capacity (1672 mAh g^{-1}) and specific energy (2600 Wh kg^{-1}), which could enhance complete reaction of electrolyte ions with sulphur to form sulphide of the ions. It is also known for its relatively low cost and environmental impact as an electrode material. Sulphur offers strong coordinate bonding with carbon/metallic surfaces due to its relatively low electronegativity. Its lower electronegativity S (2.58) accounts for capability to create more redox active sites, which improves capacity/capacitance of the electrode. Thus, sulphur-containing composite materials exhibit relatively high capacity retention and high charge/discharge cycle stability resulting from improved electrical and surface properties, and improved wettability of the electrode materials

Fig. S8 in the supporting document shows the CV curves at a scan rate of 50 mV s^{-1} in a positive potential window for RGO and RGO-S samples, respectively. The current response in the CV curves for RGO is less compared to the RGO-S. Also, RGO-S has high potential window compared to RGO as observed from Fig. S8. Hence, RGO-S has better performance compared to RGO. Fig. 4 (a) shows a rectangular CV curves of RGO-S and RGO-S/MnO$_2$ composites at different MnO$_2$ mass loading in a positive potential window range of 0.0 - 0.6 V vs Ag/AgCl at a scan rates of 50 mV s^{-1}. The overall CV curves show rectangular shape with no obvious redox peaks as indicative of EDLC dominance in the materials. From the figure it was observed that, the 100 mg of MnO$_2$ loading into the RGO-S sample proves to have higher current response as compared to the rest of the composites which is the indication of higher specific capacitance [8].

The electrochemical evaluation of the RGO-S and RGO-S/MnO$_2$ composites at different MnO$_2$ loading was further examined using the GCD curves at a specific current of 1 A g^{-1} in a positive potential range of 0.0 - 0.6 V as shown in Fig. 4 (b). The GCD behaviour corresponds well with the CV in Fig. 4 (a). The observed linear variation in the GCD curves shows that the constant charge-discharge rate reveals the features of EDLC behaviour within the material. Equation 1, was used to estimate the specific capacitance (C_s) of the RGO-S and RGO-S/MnO$_2$ composite with different mass loading of MnO$_2$, as shown below: [14,37]:

$$C_s = \frac{I_d \times \Delta t}{m \times \Delta V} \text{ [F g}^{-1}] \tag{1}$$

where, ΔV is the operating potential window in (V), I_d is the discharge current in (mA), m is the mass loading of the active material in (mg), and Δt (s) is the electrode discharge time.

Evaluated C_s corresponding to RGO-S, RGO-S/50 mg MnO$_2$, RGO-S/100 mg MnO$_2$ and RGO-S/150 mg MnO$_2$ were 75.2 F g^{-1}, 63.7 F g^{-1}, 180.4 F g^{-1} and 169.5 F g^{-1}, respectively. The calculated C_s value (63.7 F g^{-1}) for RGO-S/50 mg MnO$_2$ was observed to be lower than that of pristine RGO-S and the other composites, which is attributed to the disparity between

contributing capacitive properties of both the MnO_2 and RGO-S materials. In principle, the capacitive contribution of the respective materials in the composite is supposed to be equal or very close to each other to effect enhanced electrochemical performances. The added 50 mg of MnO_2 in the RGO-S/50 mg MnO_2 sample was not enough to facilitate effective interaction within the matrix of the composite material. This is also indicated by the sample's SEM/TEM morphology (Fig. 1(g, h and i)), which is observed to be agglomerated and in-homogenously distributed. The higher C_s observed for the RGO-S/100 mg MnO_2 composite indicates that the material responds better electrochemically as compared to the other samples. This is the indication of a good synergy between RGO-S and MnO_2 at this particular mass loading. This was also in agreement with SEM morphology for RGO-S/100 mg MnO_2 composite (Fig. 1 (j and k)) that showed well distributed porous structure. This shows that morphology plays a significant role in the electrochemical performance of the material.

The EIS technique through Nyquist plot with the frequency range 10 mHz – 100 kHz in an open circuit potential 0.0 V was used to determine the electrical resistance of the as-synthesized material. The EIS of the RGO-S and RGO-S/MnO_2 composites is displayed in Fig. 4 (c). The equivalence series resistance (ESR) which is intersect at Z' axis is a sum total of a contact resistance between the working electrode and the current collector, the interface resistance of the working electrode and ions from the electrolyte. Its values were found to be 1.5 Ω, 1.8 Ω, 0.9 Ω and 1.2 Ω for RGO-S, RGO-S/50 mg MnO_2, RGO-S/100 mg MnO_2 and RGO-S/150 mg MnO_2, respectively. It is clear that RGO-S/100 mg MnO_2 composite is having the smallest ESR value and smallest diffusion length as compared to the rest of the samples. These results still prove that RGO-S/100 mg MnO_2 composite is the best composite due to the effective incorporation of MnO_2 into RGO-S matrix.

The columbic efficiency versus cycle number is shown in Fig. 4 (d) for RGO-S, RGO-S/50 mg MnO_2, RGO-S/100 mg MnO_2 and RGO-S/150 mg MnO_2 at 5 A g^{-1}. The stability was carried

out for 2000 charge-discharge cycles. The following equation was used to evaluate the columbic efficiency C_E (%) of the material [3]:

$$C_E = \frac{t_D}{t_c} \times 100\% \qquad\qquad (2)$$

where t_c and t_D are charging-discharging time with the same current respectively.

The three-electrode measurements reveal maximum cycling stability of about 99.6 % for RGO-S/100 mg MnO$_2$ composite while 98.1 %, 97.5 % and 98.4 % for RGO-S, RGO-S/50 mg MnO$_2$ and RGO-S/150 mg MnO$_2$, respectively. The unique morphology and low ESR value of about 0.9 Ω has contributed to the higher cycling stability of RGO-S/100 mg MnO$_2$ composite.
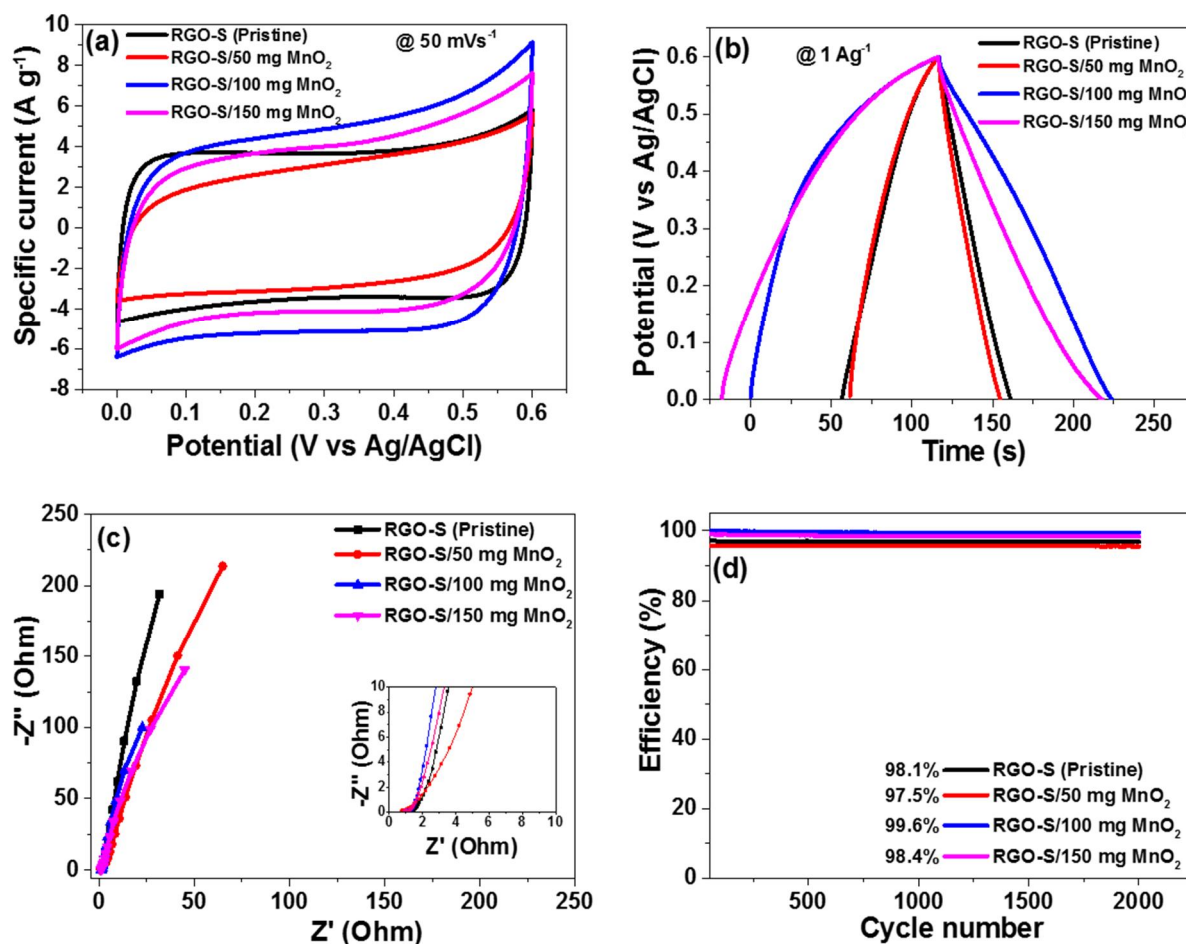

Fig. 4: (a, b) CV and GCD curves in a positive potential window for RGO-S/MnO$_2$ at different MnO$_2$ mass loading respectively and (c, d) EIS Nyquist plot and cycling stability for RGO-S/MnO$_2$ at different MnO$_2$ loading in 2.5 M KNO$_3$, respectively.

The electrochemical measurements of the RGO-S/100 mg MnO_2 composite was evaluated using CV curves at various scan rates starting from 5, 10, 25, 50 and 100 mV s^{-1} in a working potential range of 0.0 - 0.6 V vs Ag/AgCl displaying EDLC behaviour as shown in Fig. 5 (a). It was observed that as the scan rate increases, the current response increases as well, while the shape kept unchanged. Further evaluation of the GCD curves for RGO-S/100 mg MnO_2 at different specific currents is presented in Fig. 5 (b). The symmetric triangular curves at different specific currents with a small IR drop (at the beginning of the discharge curve) is observed and corresponds well with the CV curves in Fig. 5 (a). Fig. 5 (c) shows the EIS Nyquist plot for experimental and fitting, with the fitting circuit is shown as inset to the figure for RGO-S/100 mg MnO_2. The circuit shows ESR (equivalent series resistance) is in series with R_{CT} (charge transfer resistance) at high-frequency region and W (Warburg) is in parallel with Q1 (real capacitance). A mass capacitance (C3) is parallel with the leakage resistance (R_L) at low frequency region. R_{CT} represents the reactions that occurs at the interface of the electrode and electrolyte. The obtained values for ESR = 1.2 Ω and R_{CT} = 0.8 Ω from the fitting are comparable with the experimental values ESR = 0.9 Ω and R_{CT} = 0.6 Ω, respectively indicating good fitting of the Nyquist plot. The small R_{CT} = 0.8 Ω reveals fast ion transport and charge-transfer kinetics which describes good properties for capacitive material.
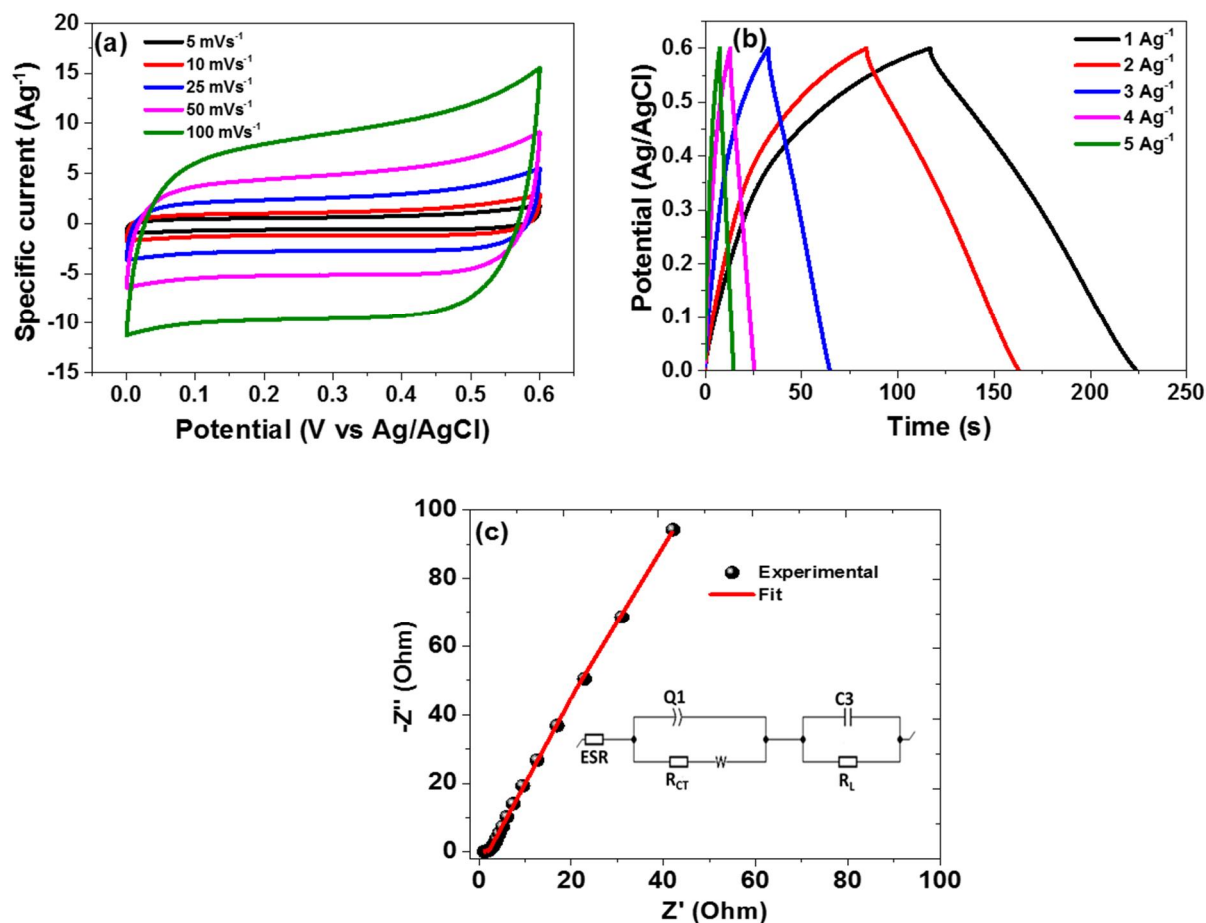
Fig. 5: (a, b) CV and GCD curves in a positive potential window at different scan rates and specific currents, respectively and (c) EIS Nyquist plot with an insert circuit for RGO-S/100 mg MnO_2 in 2.5 M KNO_3, respectively.

The as-synthesized RGO-S/100 mg MnO_2 composite material was further investigated using two-electrode measurements for the real application. The electrode was tested in both positive (as discussed above) and negative potential window and shows better performance in the positive potential window (in terms of current response) as shown in the supporting information Fig. S5 (a). Furthermore, based on CV curves in Fig. S5 (a, b), the asymmetric device could be pushed further to an extended operating potential of about 1.5 V. Therefore, the RGO-S/100 mg MnO_2 was selected as positive electrode while activated carbon from peanut shells (AC-PS) was selected as negative electrode (see Fig. S4 in the supporting information for more details) to make up the device. The choice of AC-PS was due to its compatibility in the same electrolyte with positive electrode, high pore size which easy the passage of electrolyte ions

17

and high conductivity and its detailed electrochemical properties had been discussed in our previous work [41].

The charge balance equation, $Q_+ = Q_-$ was used to balance the mass of each electrode with the charge stored on each electrode being stated as:

$$Q = C_s \times m\,\Delta V \tag{3}$$

where m (g) is the mass of active material, C_S (F g^{-1}) is the specific capacitance of the electrode based on the mass of active material, ΔV (V) is the potential window and Q (C) is the stored charge on the electrode.

The following equation (4) was used to determine the mass balance between positive and negative electrodes [46]:

$$\frac{m_+}{m_-} = \frac{C_{s-}\;\Delta V_-}{C_{s+}\;\Delta V_+} \tag{4}$$

The mass balance ratio of 1.0:2.0 obtained by using equation 4 for each electrode was 2.0 and 4.0 mg for RGO-S/100 mg MnO$_2$ and AC-PS, respectively making a total mass of 6.0 mg cm^{-2}. A filter paper soaked into 2.5 M KNO$_3$ was sandwiched between a mass of positive and negative electrode in a coin cell (Standard 2032 grade) setup.

Fig. 6 (a) shows the CV curves at 50 mV s^{-1} of RGO-S/100 mg MnO$_2$ composite and AC-PS (see Fig. S4 in supporting information for more on electrochemical properties of the AC-PS) materials used as positive and negative electrodes, respectively. Both electrodes display rectangular CV shapes revealing the properties of electric double layer capacitor (EDLC) in the 2.5 M KNO$_3$ neutral electrolyte. The fabricated hybrid device could run well at a much higher potential of up to 1.7 V, due to the synergetic effect between the two electrode materials and the use of neutral electrolyte which can still work on the high potential window. The CV curves of the asymmetric device at different scan rates are shown in Fig. 6 (b). It was observed that the synergetic effect of the combined material can be clearly revealed by the CV curves at

different scan rates, showing the contribution from the negative and positive electrodes as depicted in Figs. 6 (a and b) . Fig. 6 (c) shows the galvanostatic charge-discharge (GCD) of the asymmetric device at different specific currents of 1, 2, 3, 4 and 5 A g^{-1}.   The GCD curves displays the symmetric triangular profiles which is in accordance with the CV curves in Fig. 6 (b).

Fig. 6 (d) shows specific capacitance (C_S) evaluated from the GCD curves of the device using Eqn 1 plotted against different specific currents. The evaluated specific capacitances for the asymmetric device were recorded as 178.74, 156.99, 148.84, 142.19 and 137.76 F g^{-1} at 1, 2, 3, 4 and 5 A g^{-1}, respectively. It was observed that as the specific current increases the specific capacitances decreased slowly indicating highly reversible capacitive nature of the material (ie there was no rapid reduction of the specific capacitance as the specific current increases). This indicates high rate capability of the material which was contributed by synergy between RGO-S/100 mg MnO$_2$ and AC-PS which allowed electrolytes ions to access the material during rapid charge/discharge process. The practical application of the device was pointed out by these values. The specific energy and power densities were evaluated using Eqns. 5 and 6 below [3,46,47].

$$E_d = \frac{1}{2} C_S V^2 = \frac{C_S V^2}{7.2} \text{ [Wh kg}^{-1}]$$ (5)

$$P_d = \frac{E_d}{\Delta t} \times \mathbf{3600} \text{ [W kg}^{-1}]$$ (6)

where, C_S corresponds to the specific capacitance (F g^{-1}), V operating potential (V), Δt is discharge time (s), E_d and P_d are specific energy and power densities, respectively, with their specified units.

Fig. 6 (e) displays the so-called Ragone plot (specific energy versus specific power plot) and it found that specific energy of about 71.74 Wh kg^{-1} with its corresponding specific power of 850 W kg^{-1} was recorded for the device at 1 A g^{-1}. The fabricated asymmetric device displayed very

state specific energy versus specific power to the extent that even at a high specific current of 5 A g^{-1}, the specific energy remains as 55.30 Wh kg^{-1} with its corresponding specific power of 4250 W kg^{-1}. The fabricated device revealed higher energy and power density compared to some similar materials previously reported in the literature as shown in table 1.
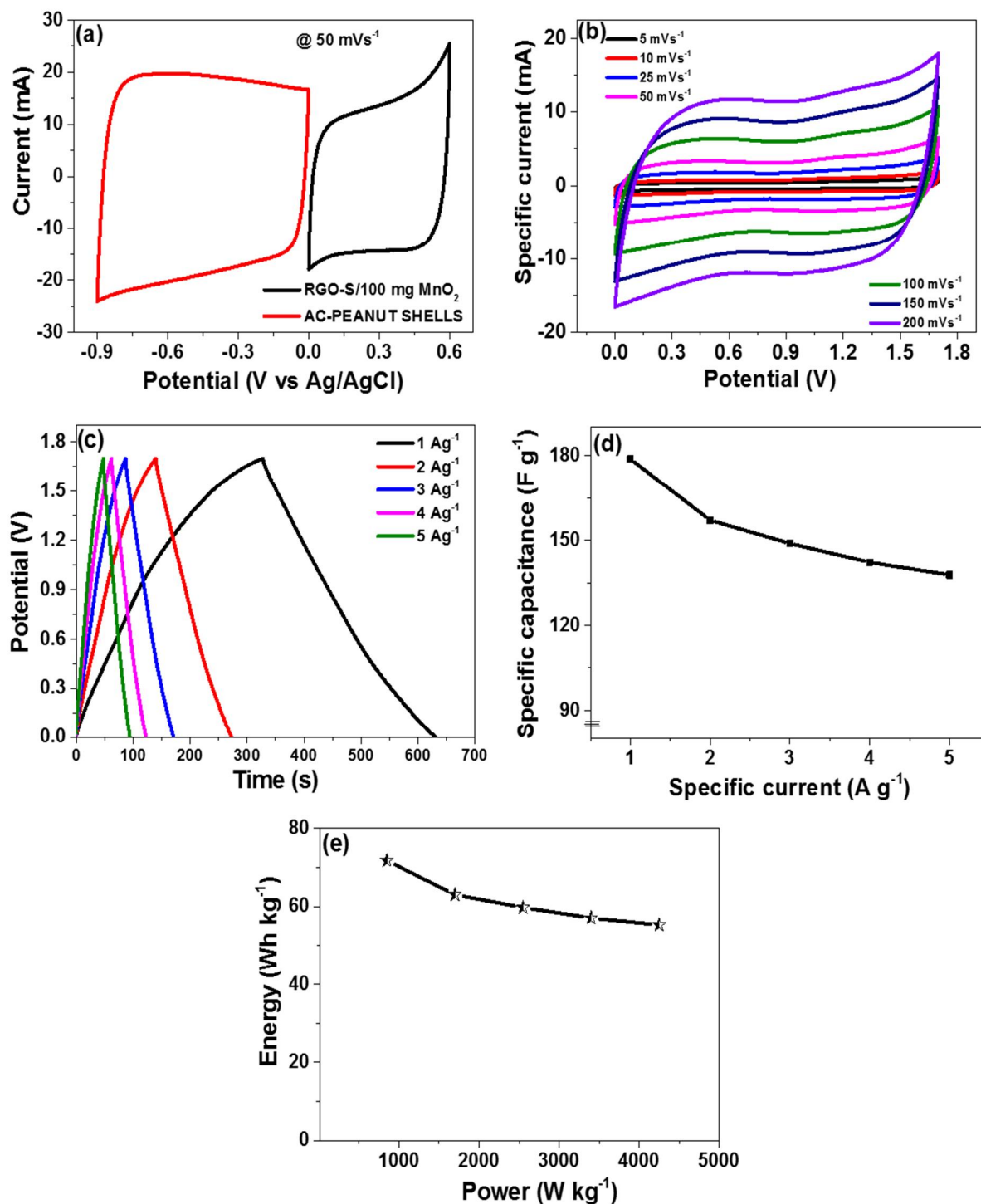

Fig. 6: RGO-S/MnO$_2$//AC-PS asymmetric device: (a) CV of positive and negative electrodes, (b) CV curves at different scan rates, (c) GCD curves at different specific currents, (f) Specific capacitance versus specific current and (e) Ragone plot in 2.5 M KNO$_3$, respectively.

Table 1: Comparisons of electrochemical performance (energy and power density) of some similar materials on RGO-S/MnO$_2$//AC-PS evaluated using two electrode cell configurations.

Electrodes (Device)	Electrolyte	Energy density	Power density	Ref.
GF/MnO$_2$//GF/MnO$_2$	1 M Na$_2$SO$_4$	34 Wh kg^{-1}	20 kW kg^{-1}	[20]
G-Υ-MnO$_2$/CNT//G-Υ-MnO$_2$/CNT	1 M KOH	43 Wh kg^{-1}	26 kW kg^{-1}	[17]
e-CMG/MnO$_2$//e-CMG	1 M Na$_2$SO$_4$	44 Wh kg^{-1}	25 kW kg^{-1}	[13]
GF/MnO$_2$//AC	1 M Na$_2$SO$_4$	51.1 Wh kg^{-1}	102.2 W kg^{-1}	[47]
MnO$_2$/rEGO//MnO$_2$/rEGO	6 M KOH	25.5 Wh kg^{-1}	45 W kg^{-1}	[48]
MnO$_2$/rGO//MnO$_2$/rGO	1 M Na$_2$SO$_4$	42.7 Wh kg^{-1}	22.5 kW kg^{-1}	[49]
MnO$_2$/CNT//AC	2 M KNO$_3$	21 Wh kg^{-1}	123 kW kg^{-1}	[50]
RGO-S/MnO$_2$//AC-PS	2.5 M KNO$_3$	71.74 Wh kg^{-1}	850 W kg^{-1}	This work

The charge-discharge cycling test was carried out at 5 A g^{-1} to determine the stability of the device. Eqn. 2 was used to estimate the columbic efficiency of the device. It was found that, the device could maintain a 94.5 % of its initial capacitance with an equivalent columbic efficiency of 99.6 % for over 10, 000 cycles as presented in Fig. 7(a). The stability test of the device was further carried out through more practical stability test known as voltage holding or floating test. The degradation of an electrochemical performance for the device can be viewed straight using this phenomenon [3]. Fig. 7 (b) displays a voltage holding for the device in a maximum working potential of 1.7 V for 90 h at 5 A g^{-1}. The device was charge-discharged for three cycles whereby the specific capacitance was monitored. The device was then held at a maximum potential of 1.7 V for 10 h intervals, then subjected to charge-discharge again for three cycles and left at that fixed potential for next 10 h. The process was repeated for up to 90 h. The capacitance decreased in the first 20 h but later became stable from 20 h to over 90 h of the aging test. This could be due to the fact that at initial stage, the electrode lacks wettability. A self-discharge (SD) test was conducted at room temperature to examine the shelve life of the asymmetric device. The device was fully charged to its peak potential of 1.7 V at 1 A g^{-1} and

then left in an open circuit potential to undergo a SD. Fig. 7 (c, d) shows that within the first 10 hours the device was able to maintain a potential of 1.45 V and 1.00 V after 72 hours. The decrease in the device voltage was associated with the decomposition of water which was used as a solvent.
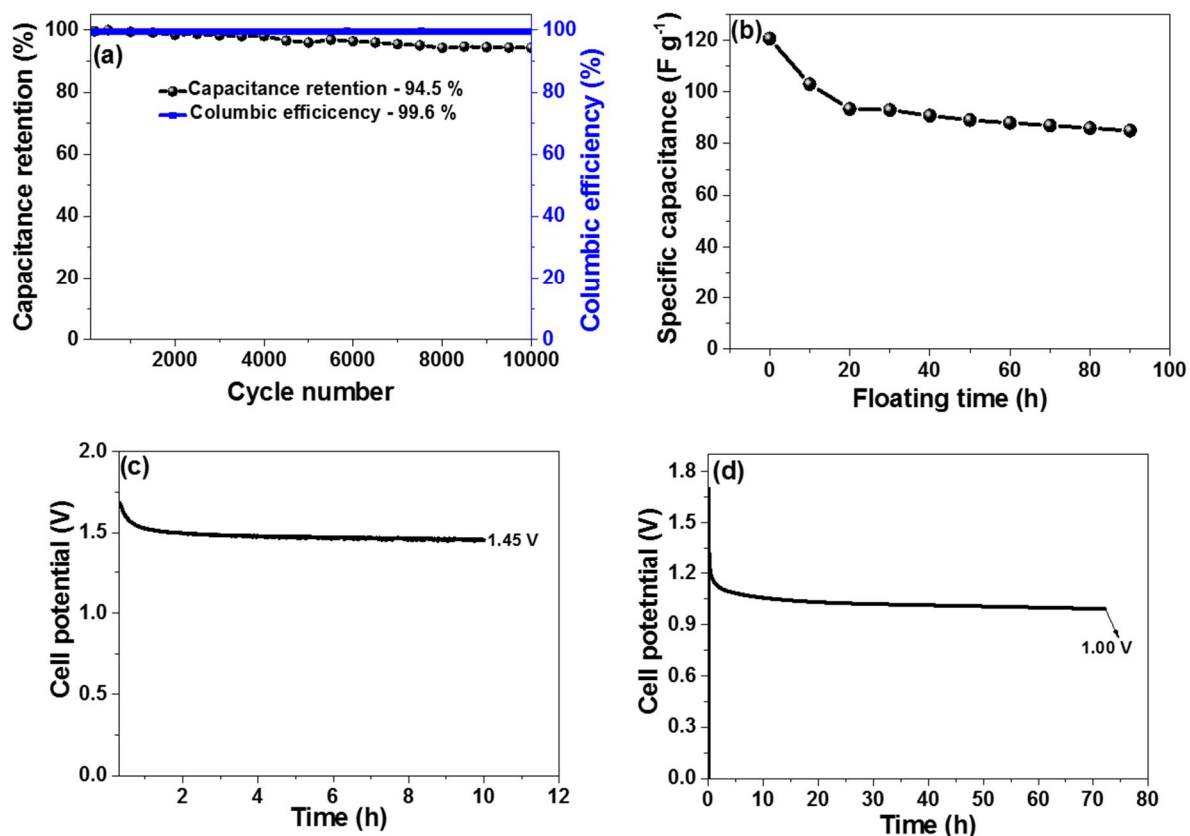

Fig. 7: (a) Capacitance retention and columbic efficiency versus cycling number, (b) Specific capacitance versus floating time, (c) Self-discharge after full charged to 1.70 V at 3 A g^{-1} within the first 10 hours and (d) Self-discharge after 72 hours for asymmetric device.
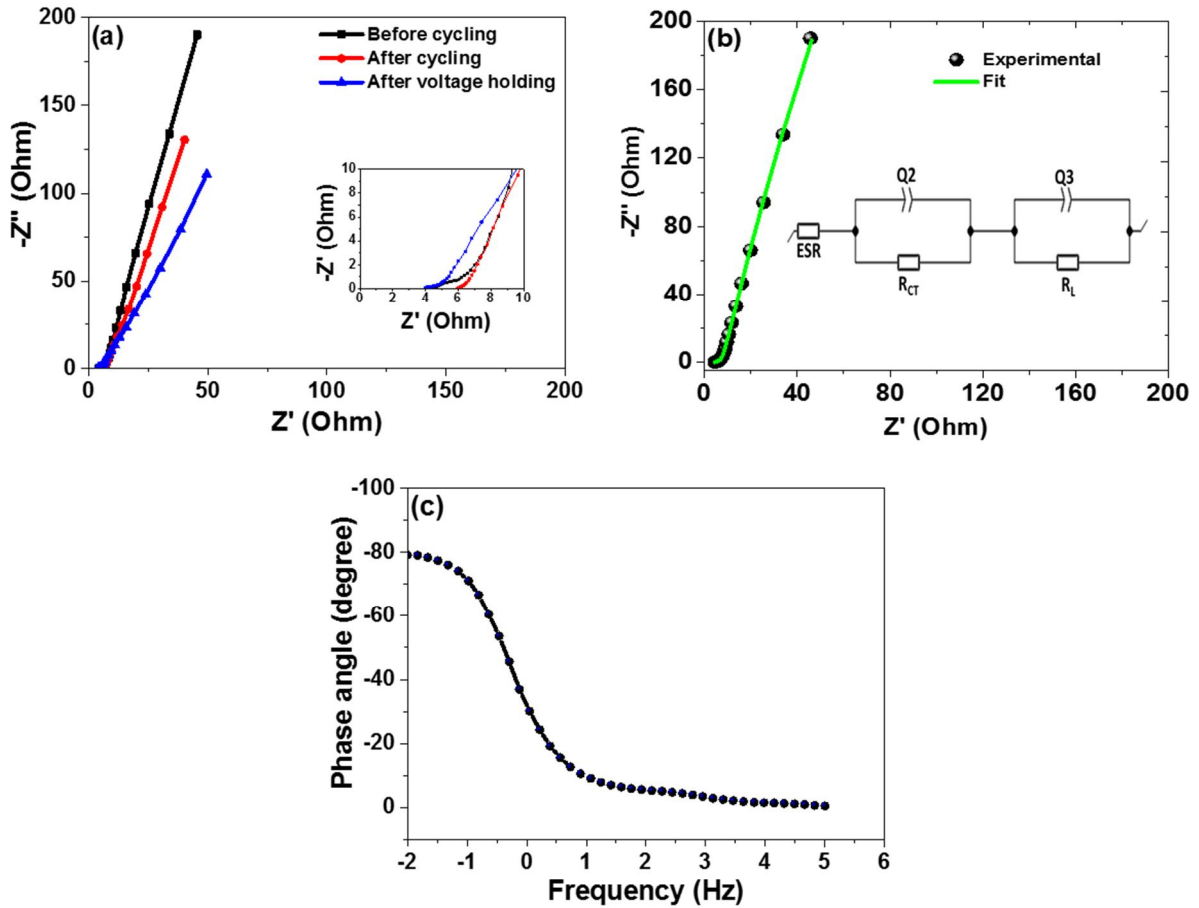
Fig. 8: (a) The EIS Nyquist plot before cycling, after cycle cycling and after voltage holding, (b) EIS Nyquist plot with an insert of equivalent electrical circuit and (c) Phase angle versus frequency for the device.

Fig. 8 (a) is a representation of the Nyquist plot of EIS test performed before cycling, after cycle stability and after voltage holding on the device. The noticed small semicircle at a high frequency region proves a low resistance and good ion diffusion at the electrode-electrolyte interface, which contributed to the supercapacitor's enhanced capacitive behaviour. It was also observed that after voltage holding test, the ESR and diffusion length reduced compared to before and after the cycling tests. This shows that after voltage holding test, the material becomes more accessible to the ions within the electrolyte. The ESR values before cycling, after cycle cycling and after voltage holding tests were recorded as ~ 5.7 Ω, 3.9 Ω and 3.7 Ω, respectively, which agree well with the observed diffusion lengths (Fig. 8 (a)). Moreover, the

EIS Nyquist plot for RGO-S/MnO$_2$//AC-PS asymmetric supercapacitor was fitted as displayed in Fig. 8 (b) with the help of Z-FIT fitting program v11.02, with the matching electrical circuit shown as inset to the figure. The equivalent circuit shows that equivalent series resistance (ESR) is connected in series with two units. The constant phase element (Q2) is parallel with charge transfer resistance (R$_{CT}$) while another constant phase element (Q3) is parallel with the leakage resistance (R$_L$) at low frequency region. The obtained values for equivalent series resistance (ESR = 5.7 Ω ~ 4.3 Ω (experimental)) and charge transfer resistance (R$_{CT}$ = 2.5 Ω ~ 2.0 Ω (experimental)) are comparable with experimental and fitting values, respectively. Moreover, Fig. 8 (c) shows the phase angle versus frequency curve with a phase angle value of about -80.4 for the device which is very close to the ideal value of -90. This result reveals that the fabricated device is performing closer to the ideal capacitive behaviour.

4. CONCLUSION

RGO-S and its MnO$_2$ composites were successfully synthesized in this study. The characterization of the samples revealed the formation of nanorods/fibers, nanosheets and nano-flower like morphology depending on the MnO$_2$ mass loading. The RGO-S/100 mg MnO$_2$ composite measured as a three electrode revealed a specific capacitance of 180. 4 F g^{-1} compared to 75.2 F g^{-1} of the RGO-S (pristine) sample at 1 A g^{-1} in 2.5 M KNO$_3$ electrolyte. The assembled RGO-S/MnO$_2$//AC-PS device delivered a high specific energy of 71.74 Wh kg^{-1} with its corresponding specific power of 850 W kg^{-1} at 1 A g^{-1}. An incredible observation was noted when the device was able to maintain a specific energy of 55.30 Wh kg^{-1} at a high specific current of 5 A g^{-1}. The capacitance retention of 94.5 % and columbic efficiency of 99.6 % up to 10, 000 cycles at 5 A g^{-1} was recorded showing outstanding stability for the device. These results show that the as-synthesized materials have great potential for supercapacitors applications.

REFERENCE

[1]   S. Sahoo, C.S. Rout, Facile Electrochemical Synthesis of Porous Manganese-Cobalt-Sulfide Based Ternary Transition Metal Sulfide Nanosheets Architectures for High Performance Energy Storage Applications, Electrochimica Acta. 220 (2016) 57–66. https://doi.org/10.1016/j.electacta.2016.10.043.

[2]   R. Ramachandran, M. Saranya, A.N. Grace, F. Wang, MnS nanocomposites based on doped graphene: simple synthesis by a wet chemical route and improved electrochemical properties as an electrode material for supercapacitors, RSC Advances. 7 (2017) 2249–2257. https://doi.org/10.1039/c6ra25457h.

[3]   O.K. Oyeniran, H. Pretoria, Synthesis and characterization of carbon-based nanostructured material electrodes for designing novel hybrid supercapacitors, (2018).

[4]   C.Y. Chen, C.Y. Fan, M.T. Lee, J.K. Chang, Tightly connected MnO 2-graphene with tunable energy density and power density for supercapacitor applications, Journal of Materials Chemistry. 22 (2012) 7697–7700. https://doi.org/10.1039/c2jm16707g.

[5]   F. Barzegar, A. Bello, D. Momodu, M.J. Madito, J. Dangbegnon, N. Manyala, Preparation and characterization of porous carbon from expanded graphite for high energy density supercapacitor in aqueous electrolyte, Journal of Power Sources. 309 (2016) 245–253. https://doi.org/10.1016/j.jpowsour.2016.01.097.

[6]   J. Zhao, G. Wang, R. Hu, K. Zhu, K. Cheng, K. Ye, D. Cao, Z. Fan, Ultrasmall-sized SnS nanosheets vertically aligned on carbon microtubes for sodium-ion capacitors with high energy density, Journal of Materials Chemistry A. 7 (2019) 4047–4054.

https://doi.org/10.1039/c9ta00141g.

[7] J.P. Cheng, J. Zhang, F. Liu, Recent development of metal hydroxides as electrode material of electrochemical capacitors, RSC Advances. 4 (2014) 38893–38917. https://doi.org/10.1039/c4ra06738j.

[8] J. Yan, Z. Fan, T. Wei, W. Qian, M. Zhang, F. Wei, Fast and reversible surface redox reaction of graphene-MnO2 composites as supercapacitor electrodes, Carbon. 48 (2010) 3825–3833. https://doi.org/10.1016/j.carbon.2010.06.047.

[9] Q. Cheng, J. Tang, J. Ma, H. Zhang, N. Shinya, L.C. Qin, Graphene and nanostructured MnO2 composite electrodes for supercapacitors, Carbon. 49 (2011) 2917–2925. https://doi.org/10.1016/j.carbon.2011.02.068.

[10] S. Ramesh, H.M. Yadav, K. Karuppasamy, D. Vikraman, H.S. Kim, J.H. Kim, H.S. Kim, Fabrication of manganese oxide@nitrogen doped graphene oxide/polypyrrole (MnO2@NGO/PPy) hybrid composite electrodes for energy storage devices, Journal of Materials Research and Technology. 8 (2019) 4227–4238. https://doi.org/10.1016/j.jmrt.2019.07.033.

[11] H. Chen, F. Yu, G. Wang, L. Chen, B. Dai, S. Peng, Nitrogen and Sulfur Self-Doped Activated Carbon Directly Derived from Elm Flower for High-Performance Supercapacitors, ACS Omega. 3 (2018) 4724–4732. https://doi.org/10.1021/acsomega.8b00210.

[12] W. Zhang, F. Liu, Q. Li, Q. Shou, J. Cheng, L. Zhang, B.J. Nelson, X. Zhang, Transition metal oxide and graphene nanocomposites for high-performance electrochemical capacitors, Physical Chemistry Chemical Physics. 14 (2012) 16331–16337. https://doi.org/10.1039/c2cp43673f.

[13] B.G. Choi, M. Yang, W.H. Hong, J.W. Choi, Y.S. Huh, 3D macroporous graphene frameworks for supercapacitors with high energy and power densities, ACS Nano. 6 (2012) 4020–4028. https://doi.org/10.1021/nn3003345.

[14] S. Ramesh, D. Vikraman, H.S. Kim, H.S. Kim, J.H. Kim, Electrochemical performance of MWCNT/GO/NiCo2O4 decorated hybrid nanocomposite for supercapacitor electrode materials, Journal of Alloys and Compounds. 765 (2018) 369–379. https://doi.org/10.1016/j.jallcom.2018.06.194.

[15] J. Zhu, J. He, Facile synthesis of graphene-wrapped honeycomb MnO 2 nanospheres

and their application in supercapacitors, ACS Applied Materials and Interfaces. 4 (2012) 1770–1776. https://doi.org/10.1021/am3000165.

[16]   L. Deng, G. Zhu, J. Wang, L. Kang, Z.H. Liu, Z. Yang, Z. Wang, Graphene-MnO2 and graphene asymmetrical electrochemical capacitor with a high energy density in aqueous electrolyte, Journal of Power Sources. 196 (2011) 10782–10787. https://doi.org/10.1016/j.jpowsour.2011.09.005.

[17]   R.B. Rakhi, W. Chen, D. Cha, H.N. Alshareef, Nanostructured ternary electrodes for energy-storage applications, Advanced Energy Materials. 2 (2012) 381–389. https://doi.org/10.1002/aenm.201100609.

[18]   P.M. Shafi, R. Dhanabal, A. Chithambararaj, S. Velmathi, A.C. Bose, α-MnO2/h-MoO3 Hybrid Material for High Performance Supercapacitor Electrode and Photocatalyst, ACS Sustainable Chemistry and Engineering. 5 (2017) 4757–4770. https://doi.org/10.1021/acssuschemeng.7b00143.

[19]   H. Chen, M.Q. Wang, Y. Yu, H. Liu, S.Y. Lu, S.J. Bao, M. Xu, Assembling Hollow Cobalt Sulfide Nanocages Array on Graphene-like Manganese Dioxide Nanosheets for Superior Electrochemical Capacitors, ACS Applied Materials and Interfaces. 9 (2017) 35040–35047. https://doi.org/10.1021/acsami.7b12069.

[20]   A. Bello, O.O. Fashedemi, J.N. Lekitima, M. Fabiane, D. Dodoo-Arhin, K.I. Ozoemena, Y. Gogotsi, A.T. Charlie Johnson, N. Manyala, High-performance symmetric electrochemical capacitor based on graphene foam and nanostructured manganese oxide, AIP Advances. 3 (2013). https://doi.org/10.1063/1.4819270.

[21]   A. Elmouwahidi, J. Castelo-Quibén, J.F. Vivo-Vilches, A.F. Pérez-Cadenas, F.J. Maldonado-Hódar, F. Carrasco-Marín, Activated carbons from agricultural waste solvothermally doped with sulphur as electrodes for supercapacitors, Chemical Engineering Journal. 334 (2018) 1835–1841. https://doi.org/10.1016/j.cej.2017.11.141.

[22]   J. Zhao, G. Wang, K. Cheng, K. Ye, K. Zhu, J. Yan, D. Cao, H.E. Wang, Growing NiS2 nanosheets on porous carbon microtubes for hybrid sodium-ion capacitors, Journal of Power Sources. 451 (2020). https://doi.org/10.1016/j.jpowsour.2020.227737.

[23]   J. Zhao, Y. Li, G. Wang, T. Wei, Z. Liu, K. Cheng, K. Ye, K. Zhu, D. Cao, Z. Fan, Enabling high-volumetric-energy-density supercapacitors: Designing open, low-tortuosity heteroatom-doped porous carbon-tube bundle electrodes, Journal of

Materials Chemistry A. 5 (2017) 23085–23093. https://doi.org/10.1039/c7ta07010a.

[24]   C. Jing, X. Song, K. Li, Y. Zhang, X. Liu, B. Dong, F. Dong, S. Zhao, H. Yao, Y. Zhang, Optimizing the rate capability of nickel cobalt phosphide nanowires on graphene oxide by the outer/inter-component synergistic effects, Journal of Materials Chemistry A. 8 (2020) 1697–1708. https://doi.org/10.1039/c9ta12192g.

[25]   T. Lin, Y. Tang, Y. Wang, H. Bi, Z. Liu, F. Huang, X. Xie, M. Jiang, Scotch-tape-like exfoliation of graphite assisted with elemental sulfur and graphene-sulfur composites for high-performance lithium-sulfur batteries, Energy and Environmental Science. 6 (2013) 1283–1290. https://doi.org/10.1039/c3ee24324a.

[26]   M. Chen, Q. Lu, S. Jiang, C. Huang, X. Wang, B. Wu, K. Xiang, Y. Wu, MnO2 nanosheets grown on the internal/external surface of N-doped hollow porous carbon nanospheres as the sulfur host of advanced lithium-sulfur batteries, Chemical Engineering Journal. 335 (2018) 831–842. https://doi.org/10.1016/j.cej.2017.11.039.

[27]   X. Zhao, H. Wang, G. Zhai, G. Wang, Facile Assembly of 3D Porous Reduced Graphene Oxide/Ultrathin MnO 2 Nanosheets-S Aerogels as Efficient Polysulfide Adsorption Sites for High-Performance Lithium–Sulfur Batteries, Chemistry - A European Journal. 23 (2017) 7037–7045. https://doi.org/10.1002/chem.201604828.

[28]   Z. Li, Y. Huang, L. Yuan, Z. Hao, Y. Huang, Status and prospects in sulfur-carbon composites as cathode materials for rechargeable lithium-sulfur batteries, Carbon. 92 (2015) 41–63. https://doi.org/10.1016/j.carbon.2015.03.008.

[29]   Q. Pang, D. Kundu, M. Cuisinier, L.F. Nazar, Surface-enhanced redox chemistry of polysulphides on a metallic and polar host for lithium-sulphur batteries, Nature Communications. 5 (2014) 3–10. https://doi.org/10.1038/ncomms5759.

[30]   C. Jing, X. Guo, L. Xia, Y. Chen, X. Wang, X. Liu, B. Dong, F. Dong, S. Li, Y. Zhang, Morphologically confined hybridization of tiny CoNi2S4 nanosheets into S, P co-doped graphene leading to enhanced pseudocapacitance and rate capability, Chemical Engineering Journal. 379 (2020) 122305. https://doi.org/10.1016/j.cej.2019.122305.

[31]   X. Liang, C. Hart, Q. Pang, A. Garsuch, T. Weiss, L.F. Nazar, A highly efficient polysulfide mediator for lithium-sulfur batteries, Nature Communications. 6 (2015) 1–8. https://doi.org/10.1038/ncomms6682.

[32] R.B. Pujari, A.C. Lokhande, A.A. Yadav, J.H. Kim, C.D. Lokhande, Synthesis of MnS microfibers for high performance flexible supercapacitors, Materials and Design. 108 (2016) 510–517. https://doi.org/10.1016/j.matdes.2016.07.038.

[33] Z. Li, J. Wang, S. Liu, X. Liu, S. Yang, Synthesis of hydrothermally reduced graphene/MnO2 composites and their electrochemical properties as supercapacitors, Journal of Power Sources. 196 (2011) 8160–8165. https://doi.org/10.1016/j.jpowsour.2011.05.036.

[34] P. Simon, Y. Gogotsi, Materials for electrochemical capacitors, Materials for Sustainable Energy: A Collection of Peer-Reviewed Research and Review Articles from Nature Publishing Group. (2010) 138–147. https://doi.org/10.1142/9789814317665_0021.

[35] O. Sadak, W. Wang, J. Guan, A.K. Sundramoorthy, S. Gunasekaran, MnO2 Nanoflowers Deposited on Graphene Paper as Electrode Materials for Supercapacitors, ACS Applied Nano Materials. 2 (2019) 4386–4394. https://doi.org/10.1021/acsanm.9b00797.

[36] T. Chen, Y. Tang, Y. Qiao, Z. Liu, W. Guo, J. Song, S. Mu, S. Yu, Y. Zhao, F. Gao, All-solid-state high performance asymmetric supercapacitors based on novel MnS nanocrystal and activated carbon materials, Scientific Reports. 6 (2016) 1–9. https://doi.org/10.1038/srep23289.

[37] F. Ochai-Ejeh, M.J. Madito, K. Makgopa, M.N. Rantho, O. Olaniyan, N. Manyala, Electrochemical performance of hybrid supercapacitor device based on birnessite-type manganese oxide decorated on uncapped carbon nanotubes and porous activated carbon nanostructures, Electrochimica Acta. 289 (2018) 363–375. https://doi.org/10.1016/j.electacta.2018.09.032.

[38] J. Yang, S. Gunasekaran, Electrochemically reduced graphene oxide sheets for use in high performance supercapacitors, Carbon. 51 (2013) 36–44. https://doi.org/10.1016/j.carbon.2012.08.003.

[39] S. Kannappan, K. Kaliyappan, R.K. Manian, A.S. Pandian, H. Yang, Y.S. Lee, J.-H. Jang, W. Lu, Graphene based Supercapacitors with Improved Specific Capacitance and Fast Charging Time at High Current Density, (2013). http://arxiv.org/abs/1311.1548.

[40] D.J. Tarimo, K.O. Oyedotun, A.A. Mirghni, ScienceDirect Sulphur-reduced graphene

oxide composite with improved electrochemical performance for supercapacitor applications, International Journal of Hydrogen Energy. (2020). https://doi.org/10.1016/j.ijhydene.2020.03.059.

[41] N.F. Sylla, N.M. Ndiaye, B.D. Ngom, D. Momodu, M.J. Madito, B.K. Mutuma, N. Manyala, Effect of porosity enhancing agents on the electrochemical performance of high-energy ultracapacitor electrodes derived from peanut shell waste, Scientific Reports. 9 (2019) 1–15. https://doi.org/10.1038/s41598-019-50189-x.

[42] H. Wang, Y. Yang, Y. Liang, J.T. Robinson, Y. Li, A. Jackson, Y. Cui, H. Dai, Graphene-wrapped sulfur particles as a rechargeable lithium-sulfur battery cathode material with high capacity and cycling stability, Nano Letters. 11 (2011) 2644–2647. https://doi.org/10.1021/nl200658a.

[43] X. Wang, T. Gao, F. Han, Z. Ma, Z. Zhang, J. Li, C. Wang, Stabilizing high sulfur loading Li–S batteries by chemisorption of polysulfide on three-dimensional current collector, Nano Energy. 30 (2016) 700–708. https://doi.org/10.1016/j.nanoen.2016.10.049.

[44] Y. Guo, J. Zhao, S. Yang, K. Yu, Z. Wang, H. Zhang, Preparation and characterization of monoclinic sulfur nanoparticles by water-in-oil microemulsions technique, Powder Technology. 162 (2006) 83–86. https://doi.org/10.1016/j.powtec.2005.12.012.

[45] J. Luo, H. Zhu, H. Fan, J. Liang, H. Shi, G. Rao, Synthesis of single-crystal tetragonal alpha-MnO 2 nanotubes, 3 (1996) 2005.

[46] T.M. Masikhwa, F. Barzegar, J.K. Dangbegnon, A. Bello, M.J. Madito, D. Momodu, N. Manyala, Asymmetric supercapacitor based on VS2 nanosheets and activated carbon materials, RSC Advances. 6 (2016) 38990–39000. https://doi.org/10.1039/c5ra27155j.

[47] Z. Fan, J. Yan, T. Wei, L. Zhi, G. Ning, T. Li, F. Wei, Asymmetric supercapacitors based on graphene/MnO2 and activated carbon nanofiber electrodes with high power and energy density, Advanced Functional Materials. 21 (2011) 2366–2375. https://doi.org/10.1002/adfm.201100058.

[48] H. Wang, Q. Fu, C. Pan, Green mass synthesis of graphene oxide and its MnO2 composite for high performance supercapacitor, Electrochimica Acta. 312 (2019) 11–21. https://doi.org/10.1016/j.electacta.2019.04.178.

[49] S. Jadhav, R.S. Kalubarme, C. Terashima, B.B. Kale, V. Godbole, A. Fujishima, S.W. Gosavi, Manganese dioxide/ reduced graphene oxide composite an electrode material for high-performance solid state supercapacitor, Electrochimica Acta. 299 (2019) 34–44. https://doi.org/10.1016/j.electacta.2018.12.182.

[50] V. Khomenko, E. Raymundo-Piñero, F. Béguin, Optimisation of an asymmetric manganese oxide/activated carbon capacitor working at 2 v in aqueous medium, Journal of Power Sources. 153 (2006) 183–190. https://doi.org/10.1016/j.jpowsour.2005.03.210.